

Research Article

Finite Control Set Model Predictive Control for Complex Energy System with Large-Scale Wind Power

Yang-Wu Shen ¹, Jin-Rong Yuan,² Fei-Fan Shen,³ Jia-Zhu Xu,⁴
Chen-Kun Li,¹ and Ding Wang¹

¹State Grid Hunan Electric Power Company Limited Research Institute, Changsha, Hunan, China

²State Grid Changde Power Supply Company, China

³Technical University of Denmark, Lyngby, Denmark

⁴Hunan University, Changsha, Hunan, China

Correspondence should be addressed to Yang-Wu Shen; shenyangwu@126.com

Received 9 April 2019; Accepted 23 June 2019; Published 28 July 2019

Guest Editor: Xiaoqing Bai

Copyright © 2019 Yang-Wu Shen et al. This is an open access article distributed under the Creative Commons Attribution License, which permits unrestricted use, distribution, and reproduction in any medium, provided the original work is properly cited.

Complex energy systems can effectively integrate renewable energy sources such as wind and solar power into the information network and coordinate the operation of renewable energy sources to ensure its reliability. In the voltage source converter-based high voltage direct current system, the traditional vector control strategy faces some challenges, such as difficulty in PI parameters tuning and multiobjective optimizations. To overcome these issues, a finite control set model predictive control-based advanced control strategy is proposed. Based on the discrete mathematical model of the grid-side voltage source converter, the proposed strategy optimizes a value function with errors of current magnitudes to predict switching status of the grid-side converter. Moreover, the abilities of the system in resisting disturbances and fault recovery are enhanced by compensating delay and introducing weight coefficients. The complex energy system in which the wind power is delivered by the voltage source converter-based high voltage direct current system is modeled by Simulink and simulation results show that the proposed strategy is superior to the tradition PI control strategy under various situations, such as wind power fluctuation and fault occurrences.

1. Introduction

To deal with energy shortage and environment pollution issues, the development of complex energy systems, which can effectively coordinate the operation with various renewable energy sources such as wind and solar power to ensure its reliability, has drawn much attention from many countries. The focus is on the wind farm due to its high efficiency of wind power utilization and no occupation of land resources [1–4]. With the increasing capacity of the wind farm and innovations of power electronic technologies, many researchers focus on applications of the voltage source converter-based high voltage direct current (VSC-HVDC) technique and require better operational performance of the converter of the VSC-HVDC system.

The model predictive control (MPC) [5–9] has been extensively applied in the control of modular multilevel

inverters [10], uninterruptible power systems [11], and neutral-point clamped converters [12] due to its advantages such as control flexibility and being free of modulators. The MPC strategies used for the control of the converter can be classified as the continuous control set MPC and the finite control set (FCS) MPC. For the continuous control set MPC, a modulator generates switching states based on the continuous output of the predictive controller. However, the FCS-MPC considers the limited number of switching states of the converter for solving optimization problems.

In [13], the MPC was applied to the low voltage ride-through (LVRT) of photovoltaic (PV) power plants to improve the transient stability of PV power plants. The proposed MPC based strategy is able to control the output current of the inverters quickly based on the reference current. After a fault in the grid, the proposed strategy can control the reactive power output of the PV power plant to

support the system voltage and improve the transient stability of the system. The simulation results show that the PV power plant is able to support the voltage with the proposed strategy in the low voltage situation.

In [14–17], the FCS MPC strategy was used to optimize the control of inverters. A mixed logical dynamical (MLD) model for inverters was proposed in [15]. By treating the MLD model as a predictive model, a FCS-MPC strategy for inverters was developed. The proposed strategy considers the discreteness of inverters and selects the switch state corresponding to the optimal objective value as the control signal for inverters to control the output voltage. The simulation and test results validate that the proposed FCS-MPC strategy can improve the output voltage quality of inverters. To improve the conventional FCS-MPC strategy, a multistep prediction FCS-MPC strategy for converters is proposed in [15], in which the optimal and suboptimal control actions are considered in one control cycle. The optimal control action is determined in a fashion that the control action is optimal in two control cycles. Simulation results show that the proposed multistep FCS-MPC scheme can improve the quality of the output voltage of the three-phase inverter and reduces the tracking error of the reference voltage as compared with the conventional FCS-MPC. In [16], the authors proposed a FCS-MPC strategy for a four-level converter to control output currents and voltages of flying capacitors. A discrete model of the converter is developed to obtain switching states. During each sampling period, the predicted variables are evaluated by an evaluation function and the optimal switching state with the minimum cost value is selected and applied to the converter. In [17], the authors proposed a simplified FCS-MPC with extended voltage vectors for two-level three-phase grid-connected converters. The proposed algorithm uses multiple voltage vectors for the prediction process to reduce the ripple in the grid current. Moreover, the proposed approach utilizes a preselection scheme along with a simplified MPC approach to reduce the number of voltage vectors used in the proposed strategy. Simulations show that the proposed strategy retains the effectiveness obtained in the case where all the voltage vectors are used, and at the same time the current ripple is not adversely affected and the control delay is effectively reduced.

Improved MPC strategies were proposed for the STATCOM and multilevel converters in [18, 19]. A novel control delay elimination for the MPC strategy was proposed in [18] for the control of the cascaded STATCOM. The MPC based optimization problem was proposed and simplified for the possible switching states. Based on the further recursion of the simplified MPC based model, the effect of control delay on the control performance is reduced. The simulation results show that the proposed delay elimination for the MPC strategy can improve current tracking control of the cascaded STATCOM and the system has strong robustness. In [19], the discrete mathematic model of the modular multilevel converter-based HVDC (MMC-HVDC) system is developed, and an improved MPC strategy is proposed for the five-level MMC. Moreover, the improved MPC strategy is combined with the voltage-sequencing algorithm to reduce computational burdens and realize the transmission power

control in the MMC-HVDC system and circulating current elimination.

In [20–23], the MPC strategies were applied to the control of electric motors. In [20], the authors proposed a MPC strategy combined with a disturbance observer (DOB) for regulating the torque of a permanent magnet synchronous motor (PMSM) without the steady state error. In the proposed strategy, the online optimal solutions can be obtained without relying on a numeric algorithm based on the property of the input matrix of the PMSM. The results show that the proposed MPC strategy ensures satisfactory torque control performance. A quasisteady MPC strategy for induction motors was proposed in [21]. By building a rolling optimization problem, the optimal switching state corresponding to the optimal voltage vector was selected as the output of the inverter. The simulations and experimental results show that the proposed strategy can reduce computational time and ensure satisfactory static and dynamic performance for torque.

However, the above researches mainly focus on the steady state and have not studied operational performance of inverters under renewable energy integration and system disturbances. To deal with the above issues, a FCS-MPC based control strategy for the VSC-HVDC system is proposed. The control strategy generates the reference value through the outer loop and compares the reference value with the predicted value obtained under a given voltage vector. Then, the switching status corresponding to the value function with the smallest difference is obtained and used in the next sampling period, which can achieve the fast tracking of the reference value. Moreover, abilities of the system in resisting disturbances and fault recovery are enhanced by compensating delay and introducing weight coefficients. The VSC-HVDC connected OWF system is modeled in the MATLAB/Simulink and simulation results validate that the proposed FCS-MPC strategy is superior to the tradition PI control strategy under various situations, such as wind power fluctuation and fault occurrences.

The contributions of this paper are summarized as follows: (1) a FCS-MPC based control strategy for the complex energy system is proposed considering the renewable energy integration and system disturbances; (2) a MPC based delay compensation technique is proposed. Compared with the conventional PI control strategy, the proposed FCS-MPC has the following advantages: (1) it is easy to tune control parameters; (2) it can realize multiobjective optimization and incorporate constraints; (3) there is no need to implement the decoupling process; (4) no PWM modulators are required.

2. Control Strategies for Wind Farm-Side VSC and Direct Driven Permanent Magnet Synchronous Generator

Figure 1 shows the typical configuration of the OWF connected to an external AC grid through the complex energy system. The complex energy system consists of the wind farm-side VSC (WF-VSC), the grid-side VSC (GS-VSC), and the DC transmission system. To ensure utilization of the

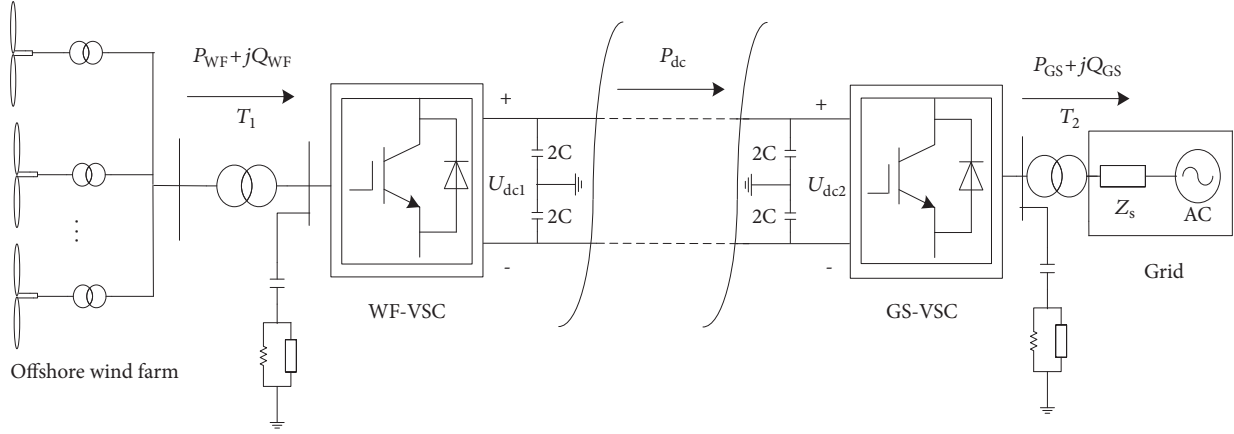


FIGURE 1: Typical configuration of the wind farm connected to an external AC grid through the complex energy system.

OWP and secure operation of the complex energy system, the GS-VSC should maintain the steady DC voltage of the DC transmission system.

2.1. Control Strategy for the WF-VSC. The mathematical model of the WF-VSC in the synchronized rotating d-q frame is formulated as below.

$$\begin{aligned} L \frac{di_{sd}}{dt} &= u_{sd} - i_{sd}R + \omega_s Li_{sq} - v_{sd} \\ L \frac{di_{sq}}{dt} &= u_{sq} - i_{sq}R - \omega_s Li_{sd} - v_{sq} \\ C \frac{du_{dc}}{dt} &= \frac{3}{2} (S_{sd}i_{gd} + S_{sq}i_{sq}) - i_{dc} \end{aligned} \quad (1)$$

where u_{sd} and u_{sq} are the d-axis and q-axis components of the three-phase voltage, respectively; i_{sd} and i_{sq} are the d-axis and q-axis components of the three-phase current, respectively; v_{sd} and v_{sq} are the d-axis and q-axis components of the voltage at the converter side, respectively; S_{sd} and S_{sq} are the d-axis and q-axis components of the switching function, respectively; ω_s is synchronized angular velocity. The direct control strategy is applied to maintain the voltage magnitude and frequency at the WF side.

The control structure of the WF-VSC is shown in Figure 2. It can be seen that the voltage magnitude and phase at the WF side are controlled through commands in d-q axis and the synchronized angular velocity of the WF-VSC. To reduce control complexity, the initial voltage angle at the WS side is set as zero and voltage magnitude components in d-q-axis are used for feedback control. The differences between the reference values and real-time values of voltage magnitude are used to obtain the modulation ratio and generate the trigger pulse.

2.2. Control Strategy for Direct Driven Permanent Magnet Synchronous Generator. The typical configuration of the direct driven permanent magnet synchronous generator (PMSG) is shown in Figure 3. The direct driven PMSG system consists

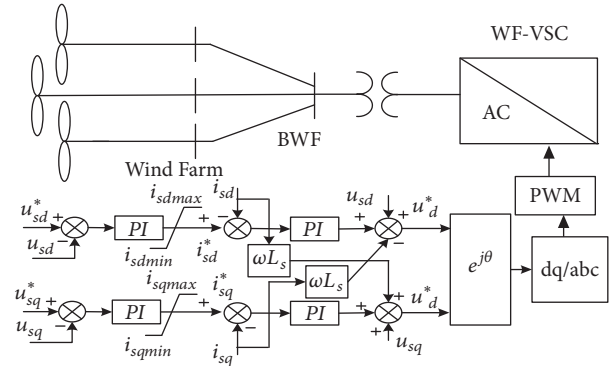


FIGURE 2: Control structure of the WF-VSC.

of the wind turbine, PMSG, generator-side converters, and grid-side converters.

The double closed loop control strategy, namely, the outer loop of angular velocity and inner loop of current, is applied to the generator-side converter to achieve the MPPT. The grid-side converter controls the DC voltage to ensure wind power integration. In this paper, the PMSG-based wind farm is represented by an equivalent single-machine model. Since the dynamic response speed of the grid-side converter is faster than the ones of the wind turbine and generator-side converters, the wind turbine, the PMSG, and generator-side converters are simplified as an equivalent voltage resource, as shown in Figure 3. Different levels of wind power output are simulated by controlling power output of the grid-side converter.

The control strategy for the grid-side converter is shown in Figure 4. In this paper, input wind power variation is simulated by controlling the grid-side converter of the PMSG because this study focuses on the verification of the abilities of the system with the proposed control strategy in resisting disturbances and fault recovery under different situations, such as wind speed variation and fault occurrence. As shown in Figure 4, the actual wind speed is simulated by the wind power generator, which generates the varying input wind power and obtains the d-axis component of the reference

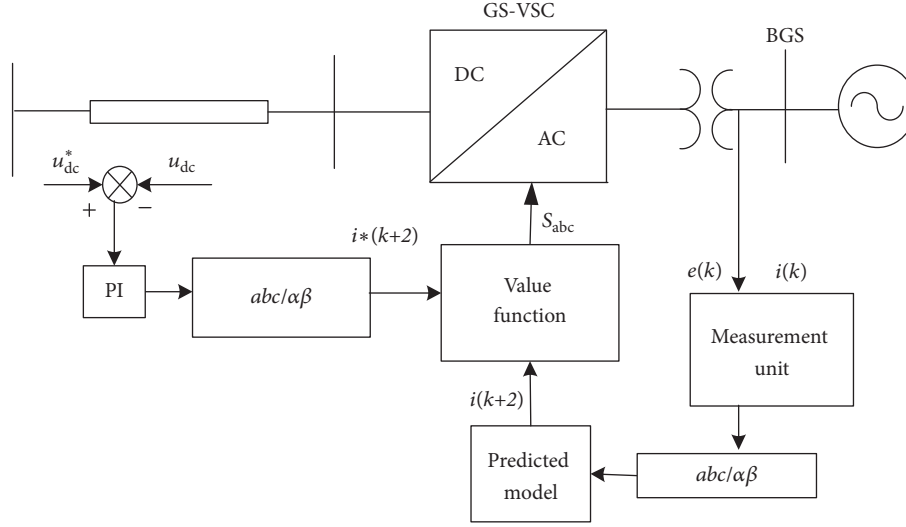


FIGURE 5: FCS-MPC based control strategy for the GS-VSC considering delay compensation.

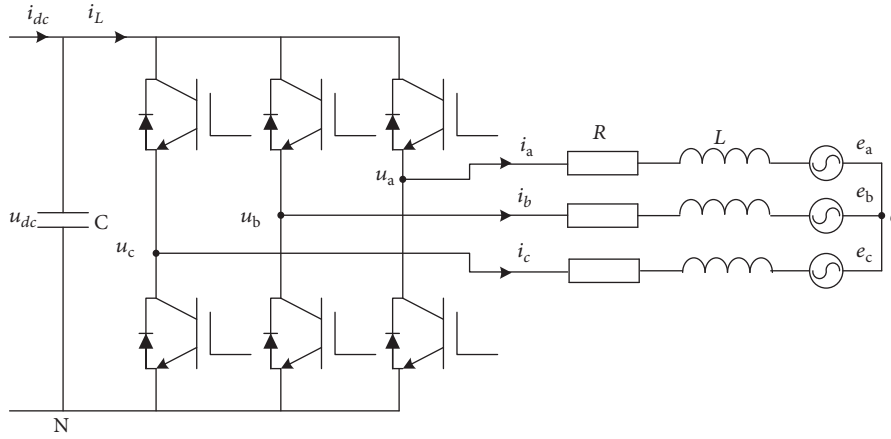


FIGURE 6: The structure of the GS-VSC.

of the converter; i_a , i_b , and i_c represent the three-phase grid current; e_a , e_b , and e_c represent the three-phase grid voltage; u_a , u_b , and u_c represent the three-phase output voltage of the converter. L is the reactance, R is the resistance, and C is the capacitance. u_{dc} , i_{dc} , and i_L are the DC voltage, DC input current, and DC output current, respectively. More details on the structure of the GS-VSC can be found in [24–27].

To derive the predicted model of the grid current, the GS-VSC should be modeled. The dynamic equation of the grid current in the three-phase stationary reference frame is as follows:

$$L \frac{d\mathbf{i}}{dt} = \mathbf{u} - \mathbf{e} - R\mathbf{i} \quad (2)$$

where \mathbf{i} is the vector of current; \mathbf{u} is the vector of output voltage of converter; \mathbf{e} is the vector of the grid voltage. Vectors \mathbf{i} , \mathbf{u} , and \mathbf{e} can be expressed as

$$\begin{bmatrix} \mathbf{i} \\ \mathbf{u} \\ \mathbf{e} \end{bmatrix} = \frac{2}{3} \begin{bmatrix} i_a & i_b & i_c \\ u_{aN} & u_{bN} & u_{cN} \\ e_a & e_b & e_c \end{bmatrix} \begin{bmatrix} 1 \\ a \\ a^2 \end{bmatrix} \quad (3)$$

where $a = e^{j2\pi/3}$; u_{aN} , u_{bN} , and u_{cN} represent the three-phase output voltage of the converter to the neutral point and can be obtained using the following equation:

$$u_{xN} = S_x u_{dc}, \quad (x = a, b, c) \quad (4)$$

where S_x is the switching function representing the switching status of each bridge arm of the converter; u_{dc} is the DC voltage. The S_x can be expressed as follows [28]:

$$S_x = \begin{cases} 0 & \text{upper arm is open, lower arm is closed} \\ 1 & \text{upper arm is closed, lower arm is open} \end{cases} \quad (5)$$

Suppose that the sampling period is T_s ; the derivative of the grid current can be discretized using the forward Euler approximation method as below:

$$\frac{di}{dt} \approx \frac{i(k+1) - i(k)}{T_s} \quad (6)$$

TABLE 1: Relation between the value function, switching status, and voltage vector.

| Value function | Switching combinations (S_a, S_b, S_c) | Voltage vectors |
|----------------|--|--|
| g_0 | 000 | $U_0 = 0$ |
| g_1 | 100 | $U_1 = 2/3u_{dc}$ |
| g_2 | 110 | $U_2 = 1/3u_{dc} + j\sqrt{3}/3u_{dc}$ |
| g_3 | 010 | $U_3 = -1/3u_{dc} + j\sqrt{3}/3u_{dc}$ |
| g_4 | 011 | $U_4 = -2/3u_{dc}$ |
| g_5 | 001 | $U_5 = -1/3u_{dc} - j\sqrt{3}/3u_{dc}$ |
| g_6 | 101 | $U_6 = 1/3u_{dc} - j\sqrt{3}/3u_{dc}$ |
| g_7 | 111 | $U_7 = 0$ |

where $i(k+1)$ and $i(k)$ are sampling current values in $k+1$ th and k -th sampling periods, respectively. Substitute (6) into (2); the predicted current can be expressed as

$$i(k+1) = \frac{T_s}{L} (u(k) - e(k)) + \left(1 - \frac{RT_s}{L}\right) i(k) \quad (7)$$

The expression of (7) in the $\alpha\beta$ coordinate system can be obtained using Clarke transformation as below:

$$\begin{aligned} \begin{bmatrix} i_\alpha(k+1) \\ i_\beta(k+1) \end{bmatrix} &= \frac{T_s}{L} \begin{bmatrix} u_\alpha(k) - e_\alpha(k) \\ u_\beta(k) - e_\beta(k) \end{bmatrix} \\ &+ \left(1 - \frac{RT_s}{L}\right) \begin{bmatrix} i_\alpha(k) \\ i_\beta(k) \end{bmatrix} \end{aligned} \quad (8)$$

where $i_\alpha(k+1)$ and $i_\beta(k+1)$ are α -axis and β -axis components of the current in $k+1$ th period, respectively; $u_\alpha(k)$ and $u_\beta(k)$ are α -axis and β -axis components of the output voltage of converter in k -th period, respectively; $e_\alpha(k)$ and $e_\beta(k)$ are α -axis and β -axis components of the grid voltage in k -th period, respectively. As shown in (8), the current of the GS-VSC in $k+1$ th period can be accurately predicted according to the current measurement of the GS-VSC in k -th period, which can achieve the fast tracking and control of the GS-VSC current and enhance the ability of the GS-VSC in resisting system disturbances.

3.2. Value Function. The main goal of the GS-VSC is to ensure power balance of the VSC-HVDC transmission system and achieve wind power integration. The control strategy of the GS-VSC is described as follows. According to the desired reference output and the current input of the GS-VSC, the output voltage vector (\mathbf{U}) of the GS-VSC can be obtained by determining the switching function value, namely, switching status, of each bridge arm of the converter. Then, based on the output voltage vector (\mathbf{U}), grid voltage vector (\mathbf{E}), and equivalent reactance Z_s , the magnitude and angle controllable three-phase current (i_a, i_b, i_c) can be obtained to control the input and output power of the GS-VSC. Therefore, it is important to determine the optimal output voltage vector (\mathbf{U}) of the GS-VSC.

It can be seen from (4) and (5) that the output voltage vector (\mathbf{U}) is determined by the switching functions of three bridge arms, namely, $S_a, S_b,$ and S_c . In the study,

it is assumed that the GS-VSC is a three-phase two-level converter. Considering there are three switching function values ($S_a, S_b,$ and S_c), there are eight possible switching states and eight corresponding voltage vectors. Moreover, since $\mathbf{U}_0 = \mathbf{U}_7$, seven possible voltage output vectors are shown in Table 1.

The traditional GS-VSC uses the double closed loop structure (outer loop of power and inner loop of current) to determine the switching functions ($S_a, S_b,$ and S_c) to control the AC voltage output and current (power output) of the GS-VSC. However, parameters of the PI controller are sensitive to the system parameters and it is difficult to tune PI parameters. In addition, the feedforward compensator term affected by the circuit parameters is required to be decoupled in the traditional control strategy. To overcome these issues, a FCS-MPC based control strategy is proposed.

FCS-MPC is a model-based closed loop control method. Based on the eight possible switching combinations and eight corresponding voltage vectors (\mathbf{U}), the predicted GS-VSC current value of the next period can be obtained using the discrete predicted model of the GS-VSC given by (8). Then, comparing the predicted value with the reference value using the value function defined in (9), the optimal switching combination corresponding to the smallest value of value function is obtained and used to generate trigger pulse, which can achieve the optimal control of the GS-VSC.

$$g = \left| i_{g\alpha}^*(k+1) - i_{g\alpha}(k+1) \right| + \left| i_{g\beta}^*(k+1) - i_{g\beta}(k+1) \right| \quad (9)$$

where $i_{g\alpha}(k+1)$ and $i_{g\beta}(k+1)$ are the real and imaginary parts of the predicted current vector in the $k+1$ period under a given voltage vector, respectively; $i_{g\alpha}^*(k+1)$ and $i_{g\beta}^*(k+1)$ are the real and imaginary parts of the predicted current vector in the $k+1$ period under a given voltage vector, respectively.

Repeat the above procedures in the following sampling periods and thus the output current of the GS-VSC is optimized and controlled over the rolling horizon. Based on the above analyses, compared with the traditional PI control-based double closed loop control strategy, the FCS-MPC strategy controls converters directly according to the limited switching combinations. As such, there is no need to implement the decoupling process and the complex PI tuning process. Moreover, no modulators are required and

multilevel constraints can be considered. In particular, there is the lowest calculation complexity when two-level converter is used.

3.3. Consideration of Delay Compensation in the Proposed Strategy. The difference between the current reference and current measurement is used to construct the objective function, namely, the value function in (9), which transforms the problem of finding the optimal modulation satisfying control targets into a problem of finding the optimal switching combination corresponding to the value function with the smallest value. However, the current reference in (9) is the value in the future period, which causes delay in the control of the GS-VSC and affects the control accuracy and response speed of the GS-VSC with the FCS-MPC strategy. To deal with this problem, this study proposes to modify the value function using the predicted current value in $k+2$ th period. The predicted function of current in $k+2$ th period is

$$i(k+2|k) = \frac{T_s}{L} (u(k+1) - e(k+1)) + \left(1 - \frac{RT_s}{L}\right) i(k+1) \quad (10)$$

where $i(k+1)$ and $i(k+2|k)$ are the predicted currents in the $(k+1)$ -th and $(k+2)$ -th periods using information collected in k -th period, respectively; $u(k+1)$ is the output voltage in the $(k+1)$ -th period; $e(k+1)$ is the grid voltage in the $k+1$ th period.

The value function considering the delay compensation is as follows:

$$\tilde{g} = \left| i_{g\alpha}^*(k+2|k) - i_{g\alpha}(k+2|k) \right| + \left| i_{g\beta}^*(k+2|k) - i_{g\beta}(k+2|k) \right| \quad (11)$$

To ensure the stability of the DC voltage under the fault occurrence and wind power fluctuation, the DC current error is introduced into the value function as below:

$$\hat{g} = \left| i_{g\alpha}^*(k+2|k) - i_{g\alpha}(k+2|k) \right| + \left| i_{g\beta}^*(k+2|k) - i_{g\beta}(k+2|k) \right| + \lambda |u_{dc}^* - u_{dc}| \quad (12)$$

where λ is the weight coefficient. The predicted value of the DC voltage is introduced to the value function to improve the stability of the DC voltage under steady state and fault occurrences.

3.4. The Algorithm of the FCS-MPC Based Control Strategy. The algorithm of the FCS-MPC based control strategy is illustrated in Figure 7 and has the following steps.

Step 1. Formulate the mathematical model of the GS-VSC based on the eight switching combinations and the relation between the switching combination and corresponding input/output voltage and current.

Step 2. Construct the discrete-time model in order to predict the values of control variables in future periods.

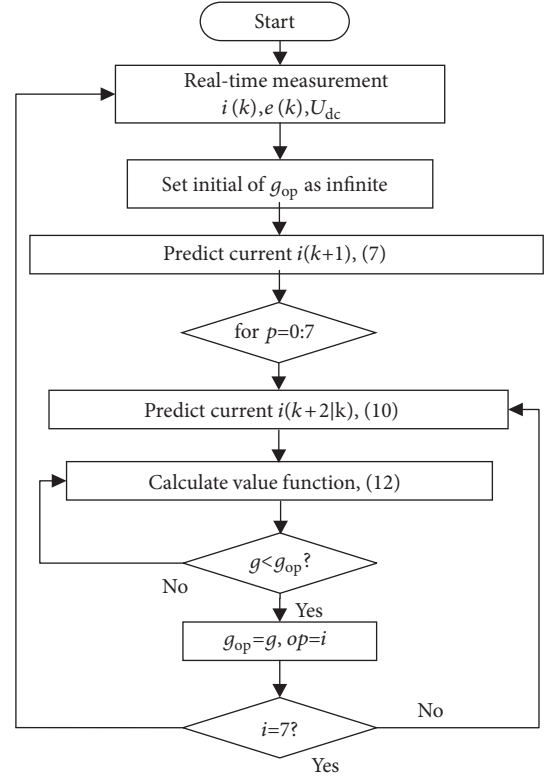


FIGURE 7: The flow chart of the FCS-MPC algorithm for GS-VSC.

Step 3. Based on the switching states currently applied, construct the discrete current model (8) in order to predict the current in $k+1$ th period.

Step 4. Predict the current in $k+2$ th period for each possible switching combination.

Step 5. Use the value function representing the expected performance of the system to evaluate all possible switching combinations.

Step 6. Choose the voltage vector corresponding to the value function with the smallest value and obtain the corresponding optimal switching combination.

Step 7. Update the status of switches based on the optimal switching combination and go back to step 2 for the next sampling period.

4. Case Studies

The VSC-HVDC connected offshore WF, as shown in Figure 1, is modeled in the MATLAB/Simulink to validate the efficiency of proposed FCS-MPC strategy. The simulation parameters are listed in Table 2.

4.1. Case 1: Wind Power Fluctuation. The comparisons between the proposed FCS-MPC strategy and traditional PI double closed loop control strategy under the wind power

TABLE 2: Simulation parameters.

| Parameters | Values |
|---|----------------|
| Rated capacity of wind farms P/MW | 4×300 |
| DC voltage u_{dc}/kV | ± 320 |
| Length of DC transmission line $/\text{km}$ | 300 |
| DC capacitor $C/\mu\text{F}$ | 75 |
| Reactance of line L/mH | 200 |
| Sampling period $T_s/\mu\text{s}$ | 50 |
| Number of time steps | 60000 |

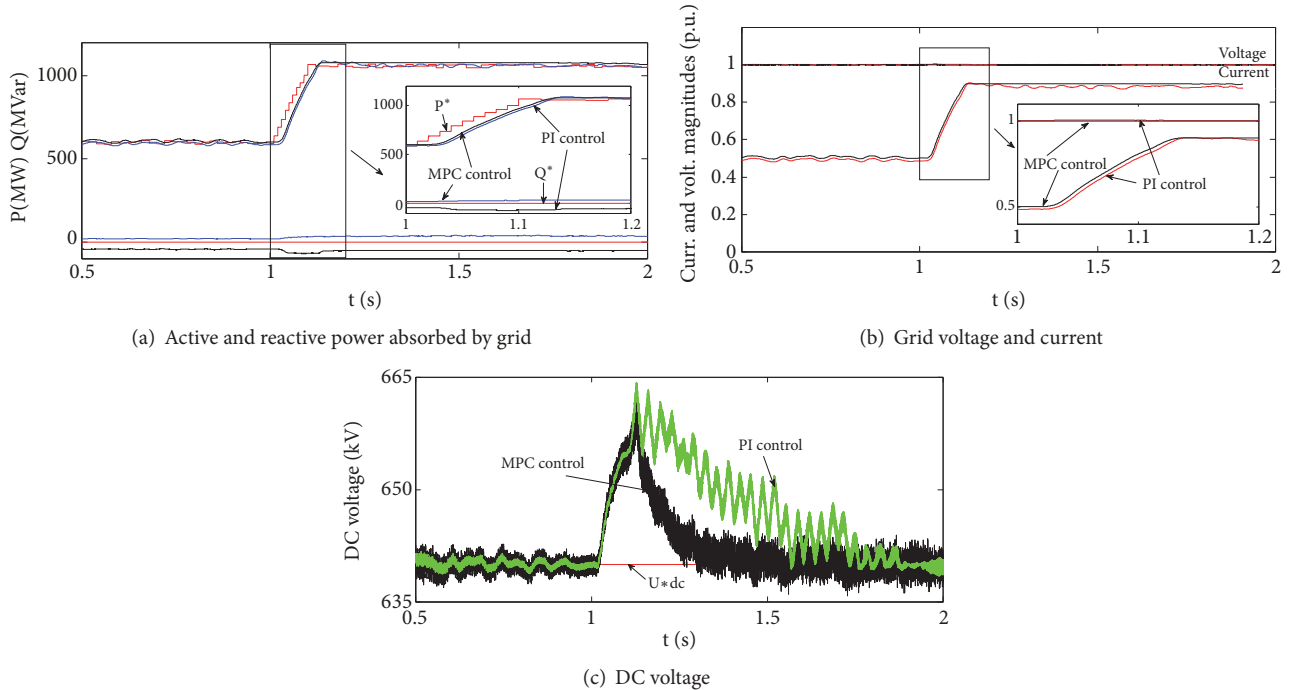


FIGURE 8: Response characteristics with two strategies under wind power fluctuation.

fluctuation are carried out in this case. The wind power output is 600MW between 0s to 1s and increases to 1100MW at 1.1s and then remains unchanged. It is assumed that the wind farm operates with the unity power factor. The simulation results of the GS-VSC with two strategies are shown in Figures 8(a)–8(c).

As shown in Figures 8(a)–8(c), the GS-VSC with two strategies can quickly respond to the WF power output variation and achieve steady wind power integration. Compared with the traditional double closed PI control strategy, the FCS-MPC adopts the single loop (outer loop of voltage) control strategy, which enables the GS-VSC to have a faster response speed and higher response accuracy, as shown in Figures 9(a)–9(b). Moreover, as shown in Figure 9(c), the DC voltage of the VSC-HVDC system is restored to the reference value more rapidly when the FCS-MPC control strategy is used because the term involved in the DC predicted voltage is considered in the value function. Therefore, the GS-VSC with the proposed FCS-MPC strategy can ensure the steady operation of the VSC-HVDC system

and has better performance under the steady state operation.

4.2. Case 2: AC Fault Occurrence at Grid Side. It is assumed that a three-phase short-circuit fault occurs at grid side at 2s and lasts for 10 ms. The response characteristic of the GS-VSC system is shown in Figures 9(a)–9(c).

As shown in Figure 9, when the traditional PI control strategy is applied to the GS-VSC, the fault occurrence has big impacts on the active/ reactive power outputs, voltage, and current outputs of GS-VSC and they are restored to the reference values slowly. In addition, due to the limited ability of the traditional PI control strategy in controlling the DC voltage, the DC voltage cannot be restored to reference value within 3s, as shown in Figure 9(c). However, when applying the proposed FCS-MPC strategy, the impacts of the fault occurrence on the outputs of GS-VSC are limited, and the active/reactive power outputs and voltage and current outputs of GS-VSC are restored to the reference values rapidly. Moreover, the DC voltage is restored to the reference value

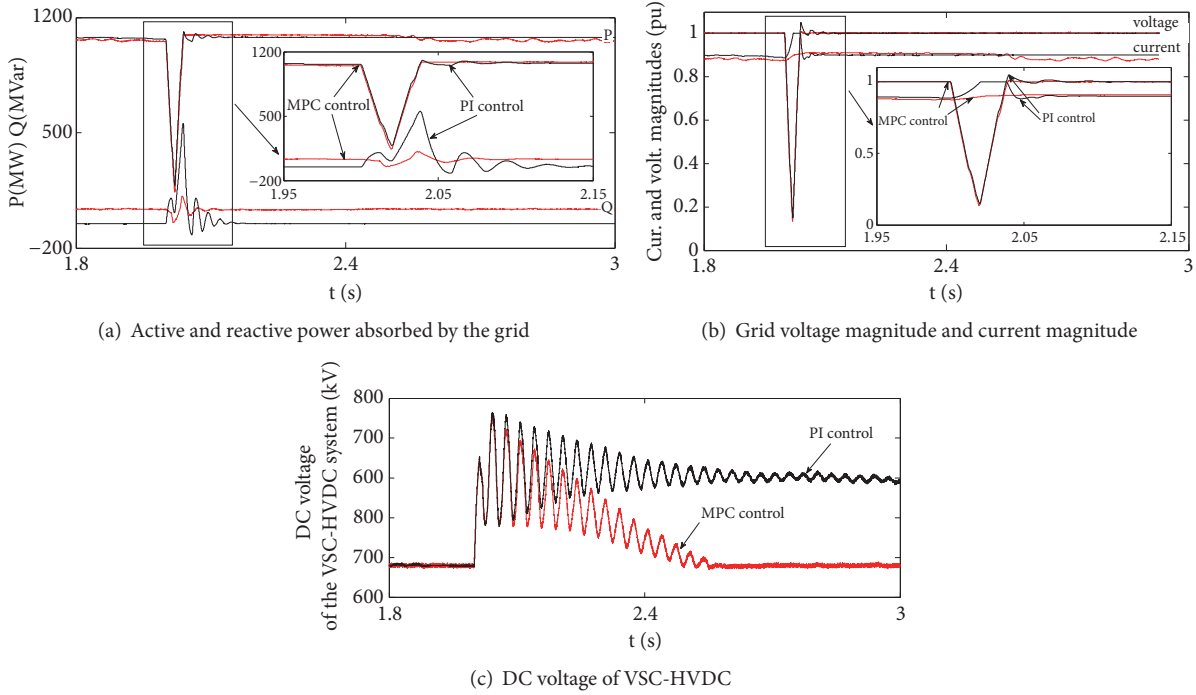


FIGURE 9: Response characteristic VSC-HVDC with two strategies under AC fault occurrence at grid side.

within 2.5s because the predictive control for the DC voltage is considered in the proposed strategy, thus improving the ability of the GS-VSC in controlling the DC voltage under fault occurrences.

4.3. Case 3: DC Fault Occurrence. It is assumed that a DC line fault occurs at the left side of the DC transmission line at 2.0s and lasts for 100 ms. The response characteristics of the VSC-HVDC system with two control strategies are shown in Figures 10(a)–10(e).

As shown in Figure 10(a), the active and reactive power decrease to -2200MW and -2000MW, respectively, in the PI control strategy while both the active and reactive power decrease to -1000MW in the proposed FCS-MPC strategy. As shown in Figures 10(b) and 10(c), the AC voltage decreases to 0.75 p.u. and the maximum transient current reaches 5 p.u. that far exceeds the maximum tolerant level of the GS-VSC. When the FCS-MPC strategy is applied to the GS-VSC, as shown in Figures 10(d) and 10(e), the AC voltage decreases to 0.9 p.u. and the maximum transient current is 2.4 p.u. It can be seen that the fluctuations of AC voltage, AC current, and active/reactive power are smaller in the proposed FCS-MPC strategy, which demonstrates the better performance of the FCS-MPC strategy.

4.4. Case 4: Grid Voltage Drops. To further validate the effectiveness of the proposed FCS-MPC strategy, the simulations are conducted when grid voltage drops. It is assumed that the grid voltage decreases from 1p.u. to 0.5 p.u. at 2.0s and the voltage remains 0.5 p.u. for 100 ms. The simulation results are shown in Figures 11(a)–11(e).

As shown in Figures 11(a)–11(e), when the proposed FCS-MPC strategy is applied, the active power decreases

to 540MW and is restored to the normal level at 2.14s. The reactive power has a very small fluctuation. The AC voltage can be restored to 1.0 p.u. rapidly after the fault is cleared and there is a very small fluctuation in AC current. However, when the PI control strategy is used, the active power decreases to 550MW and is restored to the normal level at 2.25s. The reactive power increases to 500Mvar and is restored to the normal level slowly. Likewise, the AC voltage and AC current are restored to the normal level slowly. Therefore, the FCS-MPC strategy makes the system more resistant to system disturbances.

4.5. Case 5: Comparative Analysis of Harmonic Distortion Rates of Cases 1-4. Perform the Fourier analyses under selected conditions, namely, the period (1.2s-1.4s) in Case 1 with the maximum wind power output and periods (2.3s-2.5s) in Case 2-Case 4. The distortion rates of the AC voltage and AC current under different operation conditions are shown in Table 1.

As shown in Table 3, Cases 1-4 represent the Fourier analysis results under the steady state conditions under the wind power fluctuation, under AC fault occurrence at the grid side, under DC fault occurrence, and under grid voltage drop, respectively. It can be seen from Table 1 that, in the proposed FCS-MPC strategy, the distortion rates of grid-connected voltage and current of GS-VSC are lower than 1%, which is far lower than the one in the traditional PI control strategy.

5. Conclusions

To overcome the issues in the operation of the complex energy system, this study proposes a FCS-MPC based novel

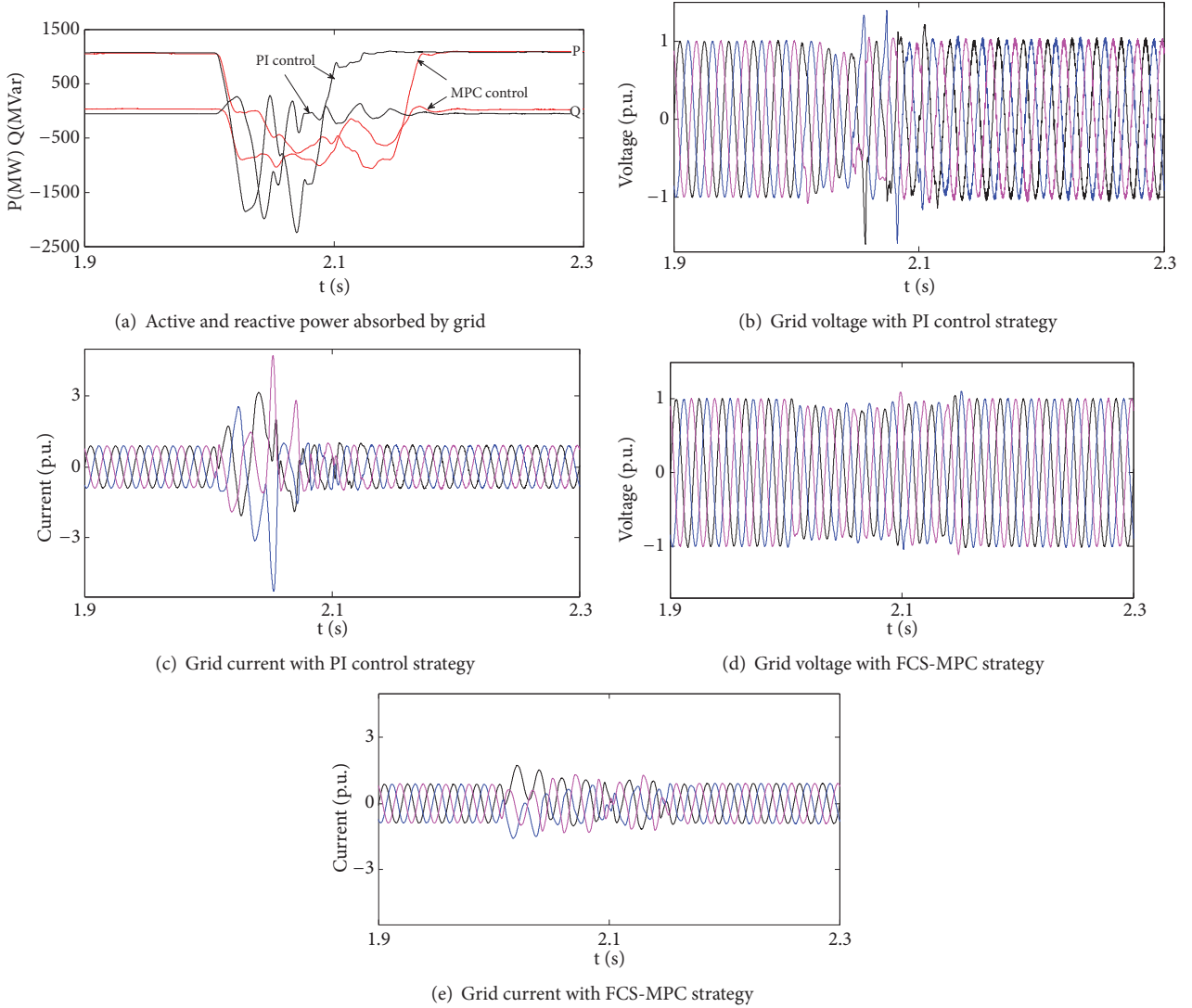


FIGURE 10: Response characteristic with two control strategies under DC fault.

TABLE 3: Harmonic distortion rates of Cases 1-4 with the FCS-MPC and PI strategy.

| | Current | | Voltage | |
|--------|---------|------|---------|------|
| | FCS-MPC | PI | FCS-MPC | PI |
| case 1 | 0.98 | 1.55 | 0.53 | 2.25 |
| case 2 | 0.62 | 2.05 | 0.48 | 2.94 |
| case 3 | 0.37 | 4.22 | 0.42 | 5.20 |
| case 4 | 0.48 | 3.59 | 0.75 | 6.94 |

control strategy. The proposed control strategy has a simple control structure, removes the inner loop of current and complex PI parameter tuning process, and achieves multiobjective optimization of the complex energy system. Moreover, the proposed control strategy considers the impact of delay and introduces the term of the DC voltage prediction in the value function to improve the stability of DC voltage control and enhances the abilities of the complex energy system in

resisting disturbances and recovering after faults. The simulation results under the wind power fluctuation, three-phase short circuit fault, and grid voltage drop validate that the system with the FCS-MPC strategy has better dynamic characteristics and parameter robustness. Moreover, the proposed strategy improves the abilities of the VSC-HVDC in resisting disturbances and fault recovery and reduces distortion rates of the grid-connected voltage and current of the GS-VSC.

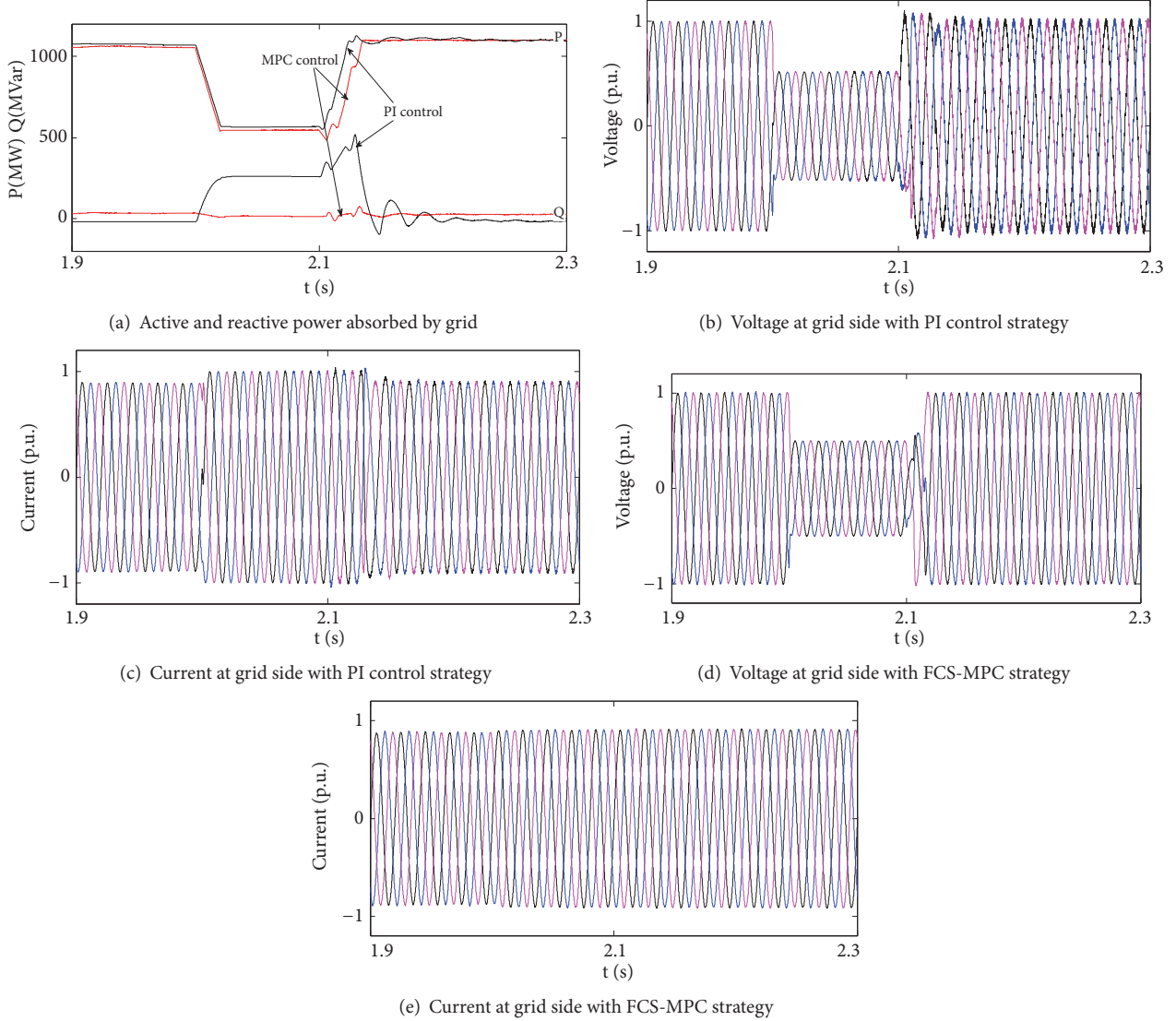


FIGURE 11: Response characteristic with two control strategies when grid voltage drops.

Nomenclature

u_{sd}, u_{sq} : d-axis and q-axis components of the three-phase voltage
 i_{sd}, i_{sq} : d-axis and q-axis components of the three-phase current
 v_{sd}, v_{sq} : d-axis and q-axis components of the voltage at the converter side
 S_{sd}, S_{sq} : d-axis and q-axis components of the switching function
 ω_s : Synchronized angular velocity
 u_a, u_b, u_c : Three-phase output voltage of the converter
 i_a, i_b, i_c : The three-phase grid current
 e_a, e_b, e_c : The three-phase grid voltage
 u_a, u_b, u_c : The three-phase output voltage of the converter
 L : Reactance
 R : Resistance

C : Capacitance
 u_{dc}, i_{dc}, i_L : The DC voltage, DC input current, and DC output current
 i, u, e : The vector of current, the vector of output voltage of converter, and the vector of the grid voltage
 u_{xN} : $x=a, b, c$, the three-phase output voltage of the converter to the neutral point
 S_x : $x=a, b, c$, the switching function representing the switching status of each bridge arm of the converter
 u_{dc} : The DC voltage of the VSC-HVDC system
 $i(k)$: The sampling current value in k -th sampling period
 $i_\alpha(k+1)$: α -axis component of the current in $(k+1)$ -th period
 $i_\beta(k+1)$: β -axis component of the current in $(k+1)$ -th period

| | |
|------------------------|---|
| $u_{\alpha}(k+1)$: | α -axis component of the output voltage of the converter in $(k+1)$ -th period |
| $u_{\beta}(k+1)$: | β -axis component of the output voltage of the converter in $(k+1)$ -th period |
| $e_{\alpha}(k+1)$: | α -axis component of the grid voltage in $(k+1)$ -th period |
| $e_{\beta}(k+1)$: | β -axis component of the grid voltage in $(k+1)$ -th period |
| $i_{g\alpha}(k+1)$: | The real part of the predicted current in the $(k+1)$ -th period under a given voltage vector |
| $i_{g\beta}(k+1)$: | The imaginary part of the predicted current in the $k+1$ th period under a given voltage vector |
| $i_{g\alpha}^*(k+1)$: | The real part of the reference current in the $(k+1)$ -th period under a given voltage vector |
| $i_{g\beta}^*(k+1)$: | The imaginary parts of the reference current in the $k+1$ th period under a given voltage vector |
| λ : | The weight coefficient |
| $i(k+2 k)$: | The predicted current value in the $(k+2)$ -th period using information collected from k -th period |
| g_{op} : | The initial value of the value function. |

Data Availability

The no secret-involvement data used to support the findings of this study are available from the corresponding author upon request.

Conflicts of Interest

The authors declare that they have no conflicts of interest.

Acknowledgments

This work has been funded by the State Grid Corporation Science and Technology Project titled “Research and Demonstration of the key technologies for application of group Electrochemical Energy Storage Power Stations in the UHV Hybrid AC/DC receiving-end power grid”.

References

- [1] O. Noureldeen and I. Hamdan, “Design of robust intelligent protection technique for large-scale grid-connected wind farm,” *Protection and Control of Modern Power Systems*, vol. 3, no. 3, pp. 169–182, 2018.
- [2] Y. W. Shen, D. P. Ke, Y. Z. Sun, D. S. Kirschen, W. Qiao, and X. Deng, “Advanced auxiliary control of an energy storage device for transient voltage support of a doubly fed induction generator,” *IEEE Transactions on Sustainable Energy*, vol. 7, no. 1, pp. 63–76, 2016.
- [3] D. Zheng, A. T. Eseye, J. Zhang, and H. Li, “Short-term wind power forecasting using a double-stage hierarchical ANFIS approach for energy management in microgrids,” *Protection and Control of Modern Power Systems*, vol. 2, no. 2, pp. 136–145, 2017.
- [4] Z. Ma, H. Chen, and Y. Chai, “Analysis of voltage stability uncertainty using stochastic response surface method related to wind farm correlation,” *Protection and Control of Modern Power Systems*, vol. 2, no. 2, pp. 211–219, 2017.
- [5] M. Soliman, O. P. Malik, and D. T. Westwick, “Multiple model predictive control for wind turbines with doubly fed induction generators,” *IEEE Transactions on Sustainable Energy*, vol. 2, no. 3, pp. 215–225, 2011.
- [6] M. D. Spencer, K. A. Stol, C. P. Unsworth, J. E. Cater, and S. E. Norris, “Model predictive control of a wind turbine using short-term wind field predictions,” *Wind Energy*, vol. 16, no. 3, pp. 417–434, 2013.
- [7] S. Kouro, P. Cortés, R. Vargas, U. Ammann, and J. Rodríguez, “Model predictive control—a simple and powerful method to control power converters,” *IEEE Transactions on Industrial Electronics*, vol. 56, no. 6, pp. 1826–1838, 2009.
- [8] A. Gosk, *Model Predictive Control of a Wind Turbine*, [M.S. thesis], Technical University, Lyngby, Denmark, 2011.
- [9] J. Rodriguez and P. Cortes, “Predictive control of power converters and electrical drives,” *IEEE Transactions on Industrial Electronics*, vol. 63, no. 7, pp. 4472–4474, 2016.
- [10] S. Rivera, S. Kouro, B. Wu et al., “Multilevel direct power control—a generalized approach for grid-tied multilevel converter applications,” *IEEE Transactions on Power Electronics*, vol. 29, no. 10, pp. 5592–5604, 2014.
- [11] G. Li and M. R. Belmont, “Model predictive control of sea wave energy converters – part i: a convex approach for the case of a single device,” *Journal of Renewable Energy*, vol. 69, pp. 453–463, 2014.
- [12] J. D. Barros, J. F. Silva, and E. G. Jesus, “Fast-predictive optimal control of npc multilevel converters,” *IEEE Transactions on Industrial Electronics*, vol. 60, no. 2, pp. 619–627, 2013.
- [13] G. Li, “Nonlinear model predictive control of a wave energy converter based on differential flatness parameterisation,” *International Journal of Control*, vol. 90, no. 1, pp. 68–77, 2017.
- [14] P. Cortés, G. Ortiz, J. I. Yuz et al., “Model predictive control of an inverter with output LC filter for UPS applications,” *IEEE Transactions on Industrial Electronics*, vol. 56, no. 6, pp. 1875–1883, 2009.
- [15] P. Cortes, A. Wilson, S. Kouro, J. Rodriguez, and H. Abu-Rub, “Model predictive control of multilevel cascaded H-bridge inverters,” *IEEE Transactions on Industrial Electronics*, vol. 57, no. 8, pp. 2691–2699, 2010.
- [16] M. Narimani, B. Wu, V. Yaramasu, C. Zhongyuan, and N. R. Zargari, “Finite control-set model predictive control (FCS-MPC) of nested neutral point-clamped (NNPC) converter,” *IEEE Transactions on Power Electronics*, vol. 30, no. 12, pp. 7262–7269, 2015.
- [17] K. S. Alam, D. Xiao, D. Zhang, and M. F. Rahman, “Simplified finite control set model predictive control (FCS-MPC) with extended voltage vectors for grid connected converters,” in *Proceedings of the 2017 Australasian Universities Power Engineering Conference, AUPEC 2017*, pp. 1–6, Australia, November 2017.
- [18] H. Jiefeng, Z. Jianguo, L. Gang, G. Platt, and D. G. Dorrell, “Multi-objective model-predictive control for high-power converters,” *IEEE Transactions on Energy Conversion*, vol. 28, no. 3, pp. 652–663, 2013.
- [19] L. Zhu, X. Fu, X. Hu et al., “Model predictive control of modular multilevel converter for HVDC system,” *Power System Protection and Control*, vol. 42, no. 16, pp. 1–8, 2014.

- [20] J. Holtz and S. Stadtfeld, "A predictive controller for the stator currentvector of AC machines fed from a switched voltage source," in *Proceedings of the International Power Electronics Conference*, pp. 1665–1675, 1983.
- [21] J. Rodriguez and P. Cortes, *Predictive Control of Power Converters and Electrical Drives*, Wiley, Hoboken, NJ, USA, 2012.
- [22] T. H. Mohaned, J. Morel, H. Bevrani, and T. Hiyama, "Model predictive based load frequency control design concerning wind turbines," *International Journal of Electrical Power & Energy Systems*, vol. 43, no. 1, pp. 859–867, 2012.
- [23] A. Calle-Prado, S. Alepuz, J. Bordonau, J. Nicolas-Apruzzese, P. Cortes, and J. Rodriguez, "Model predictive current control of grid-connected neutral-point-clamped converters to meet low-voltage ride-through requirements," *IEEE Transactions on Industrial Electronics*, vol. 62, no. 3, pp. 1503–1514, 2015.
- [24] R. Tao, F. Li, W. Chen, Y. Fan, C. Liang, and Y. Li, "Research on the protection coordination of permanent magnet synchronous generator based wind farms with low voltage ride through capability," *Protection and Control of Modern Power Systems*, vol. 2, no. 2, pp. 311–319, 2017.
- [25] Y.-W. Shen, D.-P. Ke, W. Qiao, Y.-Z. Sun, D. S. Kirschen, and C. Wei, "Transient reconfiguration and coordinated control for power converters to enhance the LVRT of a DFIG wind turbine with an energy storage device," *IEEE Transactions on Energy Conversion*, vol. 30, no. 4, pp. 1679–1690, 2015.
- [26] Y. W. Shen, L. Q. Liang, M. J. Cui, F. Shen, B. Zhang, and T. Cui, "Advanced control of DFIG to enhance the transient voltage support capability," *Journal of Energy Engineering*, vol. 144, no. 2, Article ID 04018009, 2018.
- [27] T. S. L. V. Ayyarao, "Modified vector controlled DFIG wind energy system based on barrier function adaptive sliding mode control," *Protection and Control of Modern Power Systems*, vol. 4, no. 4, pp. 34–41, 2019.
- [28] M. Alsumiri, L. Li, L. Jiang, and W. Tang, "Residue theorem based soft sliding mode control for wind power generation systems," *Protection and Control of Modern Power Systems*, vol. 3, no. 3, pp. 247–258, 2018.



Hindawi

Submit your manuscripts at
www.hindawi.com

